

1

2 **Parameterization and Evaluation of Nonhydrostatic Effect in the**
3 **Orographic Gravity Wave Drag in China Meteorological**
4 **Administration Global Forecast System (CMA-GFS) v4.0 Model**

5

6 Rongrong ZHANG^{1,2,3}, Zhenzhen AI¹, Xin XU¹, Haile XUE^{4,5}, Qiyong CHEN^{4,5}

7 ¹State Key Laboratory of Severe Weather Meteorological Science and Technology, Key
8 laboratory of Mesoscale Severe Weather/Ministry of Education, School of Atmospheric Sciences,
9 Nanjing University, Nanjing 210023, China

10 ²Jiangsu Meteorological Observatory, Jiangsu Meteorological Bureau, Nanjing 210000, China

11 ³Jiangsu Key Laboratory of Severe Storm Disaster Risk/Key Laboratory of Transportation
12 Meteorology of CMA, Nanjing 210000, China

13 ⁴State Key Laboratory of Severe Weather Meteorological Science and Technology, CMA Earth
14 System Modeling and Prediction Centre, Beijing 100081, China

15 ⁵Key Laboratory of Earth System Modeling and Prediction, China Meteorological
16 Administration, Beijing 100081, China

17

18 Correspondence: Xin Xu (xinxu@nju.edu.cn) and Haile Xue (xuehl@cma.cn)

19

20

Abstract

21

22

23

24

25

26

27

28

29

30

31

32

33

34

35

36

37

38

39

40

41

42

43

44

The China Meteorological Administration Global Forecast System (CMA-GFS) v4.0 model was upgraded to a higher resolution of 0.125° in May 2023. To be compatible with its fine resolution, the parameterization scheme of orographic gravity wave drag (OGWD) in CAM-GFS is revised herein by accounting for the nonhydrostatic effect (NHE) on the wave momentum flux of subgrid-scale orographic gravity waves. The performance of the revised OGWD scheme is then evaluated for the 10-day medium-range forecast in December 2023. Results show that the revised OGWD scheme can better capture the large-scale circulation in the Northern Hemisphere (NH), particularly in the high latitudes. The easterly (westerly) wind biases in the NH polar stratosphere (troposphere) are decreased. The underestimation of East Asia subtropical jet is also alleviated. Quantitative evaluation shows that the revised OGWD scheme reduces both the mean bias and root mean square error of 500-hPa geopotential height in the NH after the 6th forecast day, reaching 11.59% and 5.06%, respectively, by day 10. The decrease of easterly biases in the polar stratosphere is owing to the weakening of stratospheric zonal OGWD by the NHE. For the decrease of westerly biases in the NH polar troposphere, it is due to the fact that the enhanced stratospheric winds suppress the upward propagation of Rossby waves into the stratosphere, resulting in greater convergence of Eliassen-Palm flux in the mid-upper troposphere.

Keywords: orographic gravity wave drag, parameterization, global NWP medium-range forecast

45 **1. Introduction**

46 Orographic gravity wave drag (OGWD) is an important process in atmospheric
47 dynamics, arising from the interaction of airflow with complex terrain (Kim et al., 2003;
48 Teixeira, 2014). When airstream flows over mountains, it generates orographic gravity
49 waves (OGWs) which propagate vertically. *As these waves break, they transfer*
50 *momentum from the surface to higher levels* (Fritts and Alexander, 2003). This
51 momentum transfer plays a crucial role in driving the atmospheric circulation,
52 influencing both tropospheric and stratospheric dynamics (Alexander et al., 2010).

53 In numerical weather prediction (NWP) and climate models, the OGWD is
54 typically a subgrid-scale process which needs to be parameterized. Various OGWD
55 parameterization schemes have been developed over the past few decades (e.g., Palmer
56 et al., 1986; McFarlane, 1987; Kim and Arakawa, 1995; Lott and Miller, 1997; Scinocca
57 and McFarlane, 2000; Kim and Doyle, 2005) based on both linear and nonlinear OGW
58 dynamics. Their implementation has been shown to help alleviate the systematic biases
59 in both NWP and climate models, ranging from general circulation to regional climate
60 and weather (e.g., Kim, 2007; McLandress et al., 2012; Choi and Hong, 2015; Zhong
61 and Chen, 2015; Chen et al., 2016; Lu et al., 2020; Zhang et al., 2020; Li et al., 2023;
62 Xu et al., 2023; Wei et al., 2025).

63 While accurate representation of OGWD is essential for weather forecast and
64 climate simulation/projection, traditional OGWD parameterization schemes rely on the
65 assumption of hydrostatic balance which can significantly simplify the formulae of
66 OGW dynamics. This assumption is appropriate for coarse-resolution numerical models
67 where subgrid-scale OGWs are dominated by hydrostatic GWs as the dominant subgrid

68 “mountains” are large. However, as the model resolution increases, the hydrostatic
69 assumption becomes less valid because the subgrid-scale orography (SSO) becomes
70 smaller, so that the unresolved GWs have shorter wavelengths. In this situation, the
71 nonhydrostatic effects (NHEs) will exert remarkable influences on the subgrid-scale
72 OGWs. Compared with hydrostatic OGWs, nonhydrostatic OGWs experience stronger
73 horizontal dispersion of wave energy, which reduces wave amplitude and can suppress
74 wave breaking and momentum deposition into the mean flow (Smith, 1979; Klemp and
75 Durran, 1983; Zängl, 2003). These NHEs are thus critical for accurately representing
76 the dynamical impacts of subgrid-scale OGWs in high-resolution models, e.g., the
77 *state-of-the-art* global NWP models.

78 Recently, Xu et al. (2021) theoretically derived the analytical expressions for
79 the surface wave momentum flux (WMF) of nonhydrostatic OGWs generated by
80 idealized three-dimensional orography. They found that the degree of nonhydrostaticity
81 can be measured by a nondimensional parameter of Froude number which is equal to
82 the wind speed over the mountain half width and buoyancy frequency, *i.e.*, the inverse
83 of the nondimensional half-width Na/U (e.g., Zängl, 2003). Physically, this parameter
84 represents the ratio between the period of buoyancy oscillation and the time for airflow
85 travelling through the mountain. The larger the horizontal Froude number, the more
86 important the NHE is. Based upon the theoretical study, Xu et al. (2023, 2024) revised
87 the OGWD parameterization scheme developed by Kim and Doyle (2005, hereafter
88 KD05) by accounting for the NHE on the surface WMF of upward-propagating OGWs.
89 Then the new OGWD scheme was implemented in the Model for Prediction Across
90 Scales (MPAS), which was shown to improve the seasonal simulation of the

91 stratospheric polar night jet and reduce the wet biases over the western Tibetan Plateau
92 in winter. Li et al. (2024) further evaluated the revised OGWD scheme in the Weather
93 Research and Forecasting (WRF) model for short-range forecast of Northeast China
94 cold vortices (NECVs). The underestimation of the NECV intensity (in terms of
95 minimum 500-hPa geopotential height) is alleviated as the NHE decreases the lower-
96 tropospheric OGWD.

97 The China Meteorological Administration Global Forecast System (CMA-GFS)
98 is a rename of the Global/Regional Assimilation and Prediction System (GRAPES)
99 developed in early 2000s (Shen et al., 2017). Operationally running at the CMA Earth
100 System Modeling and Prediction Center, the CMA-GFS was upgraded to a new version
101 of v4.0 in May 2023, with its horizontal resolution increasing from about 0.25° to 0.125°
102 (about 13 km), along with many other improvements in the model dynamics and physics
103 (Shen et al., 2023). For instance, the convective triggering function and quasi-
104 equilibrium closure conditions are improved to reduce biases in tropics and enhance
105 forecast skill of precipitation in East Asia. In CMA-GFS, three components of [subgrid](#)
106 [scale orography effects](#) have been implemented, i.e., the blocking-flow drag (BFD), the
107 OGWD and turbulent orographic form drag (TOFD). The TOFD scheme was
108 implemented CMA-GFS based on Beljaars et al. (2004) and Xue et al. (2011) and will
109 not be further discussed as it is not relevant to the NHE effect studied in this study. The
110 BFD component based on Lott and Millor (1997, hereafter LM97) and OGWD
111 component from Kim and Arakawa (1995, hereafter KA95) were implemented in CMA-
112 GFS similar to that in Alpert (2004) and was [described](#) in Chen et al. (2016). [It is](#)
113 [noticed that in the existing implementation, nonhydrostatic effects are only partly reflected](#)

114 through a Scorer-parameter-based partitioning of the momentum stress when the model
115 grid point is located downstream of the subgrid orography. However, the launch-level
116 surface WMF itself still follows the original hydrostatic KA95 formulation. In order to be
117 compatible with its high resolution, this hydrostatic OGWD parameterization scheme
118 needs to be upgraded to account for the NHE.

119 Note that the present study extends the evaluation of the nonhydrostatic OGWD
120 scheme in the MPAS model presented in Xu et al. (2024) by transitioning it into a
121 practical, operational NWP. Although Xu et al. (2024) demonstrated the beneficial
122 impact of the revised OGWD scheme for long-term, large-scale circulation simulations,
123 its performance and value within a state-of-the-art, high-resolution global forecasting
124 system performing routine medium-range forecasts had not been tested. This work
125 provides this critical assessment using the CMA-GFS v4.0 model, with a specific focus
126 on forecast skill improvements for several quantitative metrics. The primary advance
127 lies in evaluating the revised OGWD scheme in reducing systematic forecast biases on
128 timescales directly relevant to weather prediction (1-10 days). Therefore, this research
129 bridges the gap between parameterization development and operational implementation,
130 demonstrating the tangible benefits of incorporating nonhydrostatic effects to improve
131 medium-range weather forecasting accuracy.

132 The remainder of the paper is organized as follows. Section 2 firstly introduces
133 the revision of the OGWD parameterization scheme and then describes the setup of the
134 numerical experiments. Section 3 gives an overall evaluation for the medium-range
135 forecast of large-scale atmospheric circulation by the CMA-GFS model. The NHE

136 effects on parameterized OGWD and large-scale circulation are examined in section 4.
 137 Finally, the paper is summarized in section 5 along with discussions.

138

139 **2. OGWD parameterization scheme and numerical experiments**

140 a. Revision of the KA95 OGWD parameterization scheme

141 The KA95 OGWD considers various aspects of the SSO including its standard
 142 deviation (σ_h), orographic asymmetry (OA) and orographic convexity (OC). The
 143 surface WMF of OGWs is given by

$$144 \quad \tau_0 = \rho_0 E \frac{m}{\lambda_{eff}} G \frac{|V_0|^3}{N_0}, \quad (1)$$

145 where

$$146 \quad E = (OA + 2)^{C_E \frac{Fr_0}{Fr_c}}, m = (1 + L_x)^{OA+1}, G = \frac{Fr_0^2}{Fr_0^2 + C_G OC^{-1}}, Fr_0 = \frac{\sigma_h N_L}{|V_L|}. \quad (2)$$

147 The variables ρ_0 , $|V_0|$ and N_0 are the low-level (from the surface to $2\sigma_h$) mean air
 148 density, horizontal wind speed and buoyancy frequency. The parameter m denotes the
 149 “number of mountains” within the grid cell, characterizing the total volume of SSO
 150 associated with the orography length (L_x). The coefficient λ_{eff} acts as a tunable
 151 parameter denoting the effective grid length. The transition function G is an
 152 enhancement factor for sharp mountains as OC is large. This scheme also considers the
 153 effects of low-level wave breaking and/or lee wave trapping through the factor E , which
 154 is a function of the shape and location of the SSO within the model grid cell (i.e., OA),
 155 and the flow nonlinearity (i.e., $Fr_0 = \frac{Nh_0}{U}$). The two empirical constants are set to $C_E =$
 156 0.8 and $C_G = 0.5$, which are obtained empirically through a series of numerical
 157 simulations conducted in Kim and Arakawa (1995).

158 The surface WMF is transported upward level by level until reaching the model
 159 top or critical level. At each model level, airflow instability is checked according to the
 160 hypothesis of wave saturation (Lindzen, 1981) and wave-breaking (Miller and Palmer,
 161 1986).

162 Once the subgrid-scale OGWs saturate and break, they will exert a body force
 163 on the mean flow through the deposition of wave momentum, namely,

$$164 \quad \frac{d\mathbf{V}(z)}{dt} = \frac{1}{\rho(z)} \frac{\partial \boldsymbol{\tau}(z)}{\partial z}. \quad (3)$$

165 where $\mathbf{V}(z)$ and $\boldsymbol{\tau}(z)$ are the mean flow velocity and the WMF at height z , respectively.
 166 Note that both the directions of $\mathbf{V}(z)$ and $\boldsymbol{\tau}(z)$ are parallel to the mean flow at the low
 167 level (i.e., \mathbf{V}_L). Readers are referred to KA95 for more details about the scheme.

168 The hydrostatic KA95 scheme above is revised by taking into account the NHE
 169 on the surface WMF of OGWs, i.e.,

$$170 \quad \tilde{\boldsymbol{\tau}} = \boldsymbol{\tau}_0 [1 + NHE(Fr)]. \quad (4)$$

171 $\tilde{\boldsymbol{\tau}}$ represents the nonhydrostatic surface WMF, where the NHE correction depends only
 172 on the horizontal Froude number $Fr = \frac{|\mathbf{v}_0|}{N_0 L_x}$

$$173 \quad NHE(Fr) = -\frac{9}{8} Fr^2 + e^{-2Fr^{-1}} \left(-\frac{5}{4} Fr^{-2} - \frac{1}{2} Fr^{-1} + \frac{5}{4} + \frac{9}{4} Fr + \frac{9}{8} Fr^2 \right). \quad (5)$$

174 Eq. (5) is adopted from Xu et al. (2021) for three-dimensional isotropic terrain. Specifically,
 175 the nonhydrostatic correction is defined as the ratio of the analytically derived
 176 nonhydrostatic surface WMF to its hydrostatic counterpart, which yields an algebraic
 177 correction factor depending only on the horizontal Froude number. Note that the
 178 horizontal Froude number is different from the traditional Froude number Fr_0 above
 179 which measures the flow nonlinearity. While Xu et al. (2021) have derived the fully

180 NHE for anisotropic terrain, the expressions involve complicated integrals that are not
181 suitable for practical use in parameterization [cf. their Eqs. (14) to (17)]. Xu et al. (2021)
182 demonstrated that terrain anisotropy only has a very weak influence on the NHE, so the
183 expression of NHE for isotropic terrain, i.e., Eq. (5), is used because of simplicity, since
184 only algebraic manipulations are involved. This is in agreement with Xu et al. (2023,
185 2024) and Li et al. (2024).

186

187 b. Setup of numerical experiments

188 The CMA-GFSv4.0 dynamical core is based upon the nonhydrostatic and
189 shallow atmospheric governing equations in spherical polar coordinates with full
190 physics packages (Shen et al., 2020). It adopts a regular latitude-longitude grid of
191 $0.125^\circ \times 0.125^\circ$ with *C*-grid staggering. In the vertical, a terrain-following height-based
192 grid is utilized along with Charney-Phillips staggering. There are 87 vertical levels,
193 with the model top located at 73 km. For model physics, the Liu-Ma microphysics
194 scheme (Ma et al., 2018) is employed, along with the RRTMG longwave and shortwave
195 radiation schemes (Morcrette et al., 2008), the MRF planetary boundary layer scheme
196 (Chen et al. 2020; Hong and Pan 1996), the CoLM land surface model (Dai et al., 2003),
197 NSAS convection scheme (Han and Pan, 2011; Liu et al., 2015), the combined KA95
198 OGWD and LM97 FBD parameterization scheme (Chen et al., 2016), and [modified](#)
199 Beljaars's TOFD scheme (Xue et al., 2011).

200 In order to examine the impact of the revised OGWD scheme on the medium-
201 range forecast, two sets of numerical simulations (i.e., EXP_CTL and EXP_NHE) are
202 conducted with different OGWD parameterization schemes, using the original KA95

203 scheme and the revised nonhydrostatic one, respectively. Both experiments consist of 31
204 individual forecasts, each initialized at 00 UTC for the days from 1 to 31 December 2023.
205 Herein, a winter month is chosen because the OGWD, which is mainly located in the
206 Northern Hemisphere (NH) given the pronounced orography, is the strongest in this
207 season (e.g., Xu et al. 2020; Lu et al. 2024). In each experiment, the CMA-GFS model
208 is integrated for 10 days, i.e., medium-range forecast, with 6-hr output interval. The
209 model initial conditions are derived from the $0.25^\circ \times 0.25^\circ$ ECMWF Reanalysis v5 (ERA5)
210 dataset (Hersbach et al., 2020), which are also used as reference for the evaluation of the
211 CMA-GFS forecasts. Although the horizontal resolution of ERA5 is coarser than that of
212 the CMA-GFS v4.0 simulations, ERA5 is adopted here as the verification reference
213 because it is a dynamically consistent reanalysis constrained by a broad range of
214 assimilated observations. In this study, ERA5 is not used to resolve the non-hydrostatic
215 subgrid-scale orographic gravity waves themselves. Instead, it serves as a benchmark for
216 evaluating the large-scale circulation response and medium-range forecast skill associated
217 with the revised OGWD parameterization.

218

219 **3. Evaluation of the medium-range forecast**

220 *a. Atmospheric circulation*

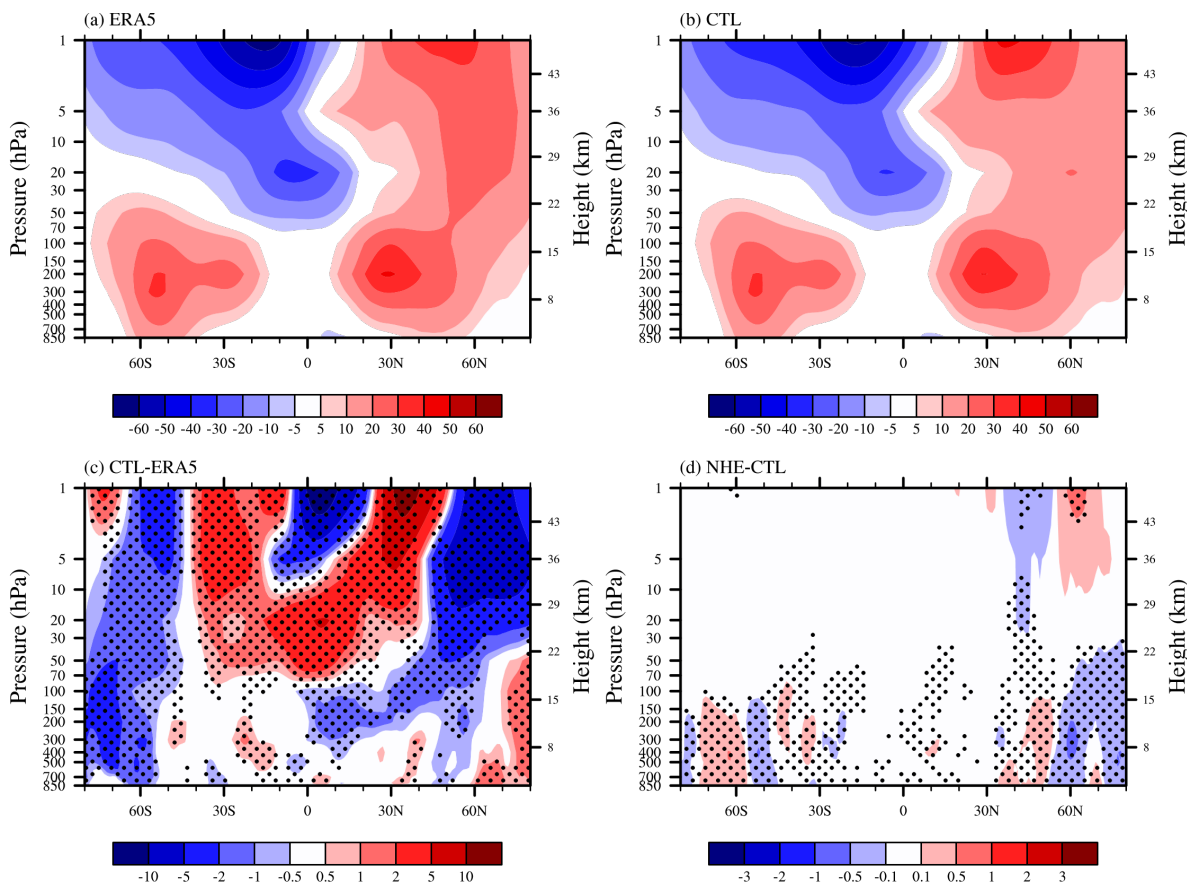
221 Figure 1 shows the zonal-mean zonal wind composited from the day 10 forecast
222 output of the 31 simulations initialized at 00 UTC on 1-31 December 2023. Accordingly,
223 the valid times of these day-10 forecasts span 10 December 2023 to 10 January 2024 (i.e.,
224 the 10th day of the medium-range forecast). In the winter of NH, as revealed by the
225 ERA5 reanalysis (Fig. 1a), there is a subtropical jet in the midlatitudes troposphere and

226 [stratosphere](#), with the jet core located at about 200 hPa and 30°N. The maximum zonal
227 wind speed exceeds 35 m s⁻¹. In the stratosphere of high latitudes, there is another wind
228 maxima near 1 hPa and 60°N, which is the well-known polar-night jet (e.g., Kim, 2007)..
229 In the Southern Hemisphere (SH), which is in summer, there is also a [upper tropospheric](#)
230 [lower stratospheric jet](#) but relatively weaker and lower than in the NH. The SH jet core
231 is located at about 50°S, with a secondary one near 30°S. [During austral summer, the](#)
232 [SH stratosphere is dominated by easterlies, which is distinctly different from the NH.](#) With
233 a center located near 1 hPa and 20°S, the stratospheric easterlies extend downward and
234 equatorward to the tropics. An easterly jet of over -30 m s⁻¹ can be found near 20 hPa
235 and 5°S.

236 Figure 1b is similar to Figure 1a but for the zonal-mean zonal winds obtained in
237 the EXP_CTL experiment. In general, the CMA-GFS model can capture the overall
238 pattern of the zonal-mean zonal winds, such as the tropospheric westerly jets in both
239 hemispheres and the easterly winds in the SH stratosphere. The polar night jet in the
240 NH, however, is underestimated by the model, with the jet core shifted southward by
241 about 10 latitudes. As shown in Fig. 1c, there are notable easterly biases of over -5 m
242 s⁻¹ in the stratosphere of the NH high latitudes (north of 50°N). By contrast, westerly
243 biases are present in the upper stratosphere of the NH midlatitudes (25°N-50°N) which
244 can exceed 10 m s⁻¹, extending downward and equatorward to the lower stratosphere of
245 the tropics. [Similarly](#), the zonal-mean zonal winds [in the NH troposphere](#) are
246 overestimated in the Arctic region, but with easterly biases in the mid-lower latitudes.
247 In the SH, the stratospheric easterlies are shifted northward, leading to westerly biases
248 in the mid-lower latitudes (40°S-5°S) and easterly biases in the tropics and lower

249 latitudes of the NH (5°S-20°N). In the high latitudes, there are predominantly easterly
250 biases in both troposphere and stratosphere except in the upper stratosphere [over the](#)
251 [polar cap](#).

252 When taking into account the NHE in the OGWD parameterization scheme, the
253 CMA-GFS model can better capture the large-scale circulation. Figure 1d presents the
254 differences between the zonal-mean zonal winds in the two numerical experiments (i.e.,
255 EXP_NHE minus EXP_CTL). In the stratosphere above ~10 hPa, positive and negative
256 wind differences are found to the north and south of 60°N, respectively, which are just
257 opposed to the wind biases in Figure 1c. It suggests that both the magnitude and location
258 of the polar night jet are improved. For example, the [NH](#) easterly biases in the mid-
259 upper stratosphere (~10 hPa to 1 hPa) are reduced by about 3%. The westerly biases in
260 the troposphere of Arctica region are also reduced, which reaches up to about 42% of
261 the total bias. [At the same time, the easterly wind biases in the mid-latitude troposphere](#)
262 [have also reduced](#).



263

264 Figure 1. Vertical distributions of zonal-mean zonal wind (units: m s^{-1}) averaged in the
 265 period of 10 December 2023 to 10 January 2024 obtained from (a) ERA5 and (b)
 266 EXP_CTL, with their difference (i.e., EXP_CTL minus ERA5) given in (c). (d) is
 267 similar to (c) but for the difference between the two experiments of EXP_NHE and
 268 EXP_CTL (i.e., EXP_NHE minus EXP_CTL). Stippling in (c) and (d) denote
 269 differences statistically significant at the 95% confidence level.

270

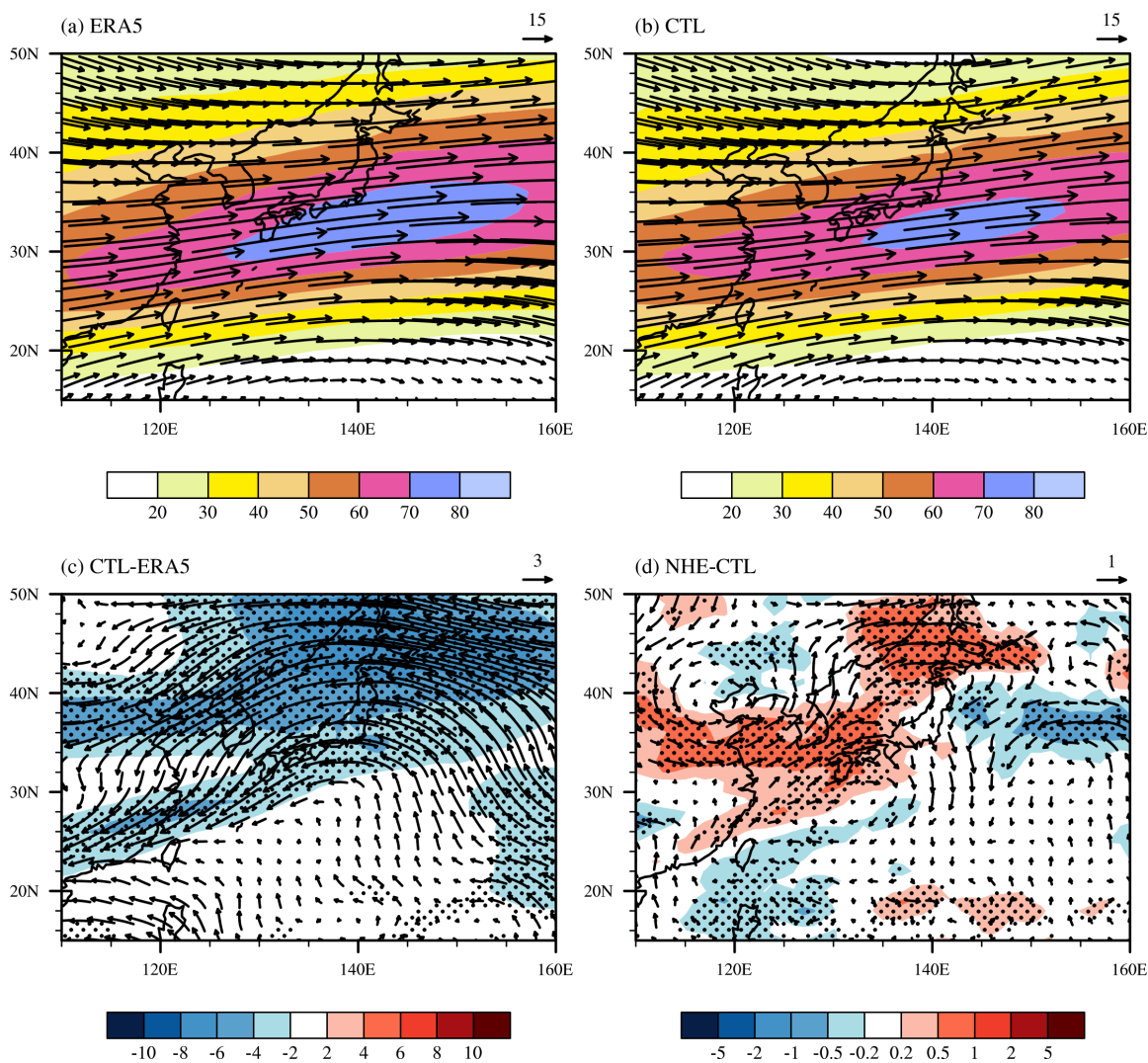
271 For the zonal-mean zonal wind biases in the SH stratosphere, they are hardly
 272 alleviated, however. This is because the stratospheric OGWD is very weak in summer
 273 (see Fig. 5a of Xu et al. 2024; see also Fig. 3 below), given the absorption of OGWs at
 274 the critical level (Booker and Bretherton, 1967), that is, the zero-wind level between
 275 the tropospheric westerlies and the stratospheric easterlies (Fig. 1a). The easterly biases
 276 in the troposphere of the high latitudes are reduced, especially around 60°S .

277 Although there is no significant improvement for the zonal-mean zonal wind in
278 the NH mid-lower latitudes (Fig. 1d), the wind circulation can be improved regionally,
279 such as the East Asia subtropical jet (EASJ). Figure 2a shows the horizontal wind field
280 and speed at 200 hPa averaged in the period of 10 December 2023 to 10 January 2024
281 from the ERA5 reanalysis. In boreal winter, the EASJ stretches from about 110°E to
282 160°E in the latitudes between about 25°N and 45°N. The jet core is located near Japan,
283 showing a high wind speed of over 70 m s⁻¹. The simulated EASJ in the EXP_CTL
284 experiment generally aligns well with the ERA5 reanalysis, in terms of its location and
285 orientation (Fig. 2b). But the jet intensity is underestimated, showing easterly biases of
286 over -4 m s⁻¹ (Fig. 2c). In the EXP_NHE experiment, the underestimation of the EASJ
287 is alleviated, with the mean bias decreased by about 6% (Fig. 2d).

288

289

290



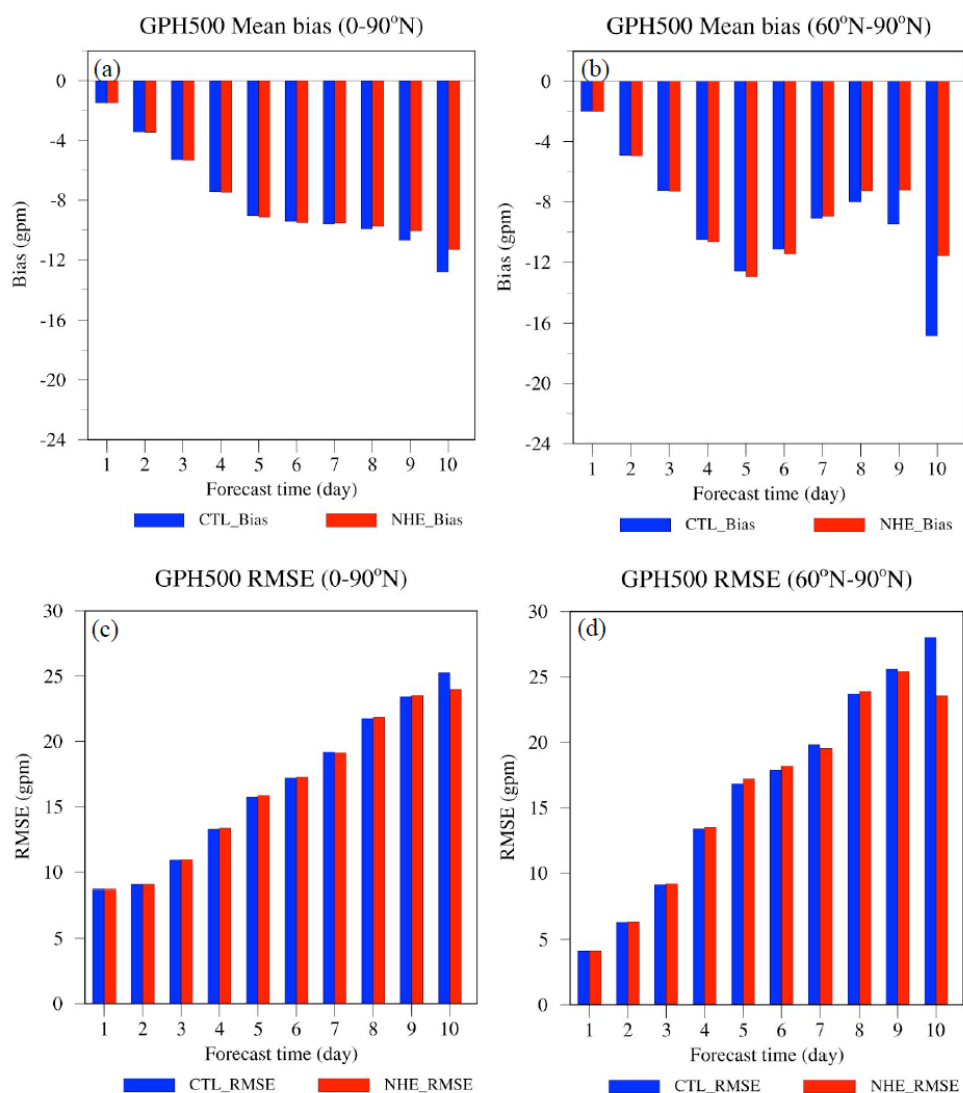
291

292 Figure 2. Horizontal distributions of wind speed (shading; units: m s^{-1}) and wind field
 293 (arrow) at 200 hPa averaged in the period of 10 December 2023 to 10 January 2024
 294 obtained from (a) ERA5 and (b) EXP_CTL, with their difference (i.e., EXP_CTL minus
 295 ERA5) given in (c). (d) is similar to (c) but for the difference between the two
 296 experiments of EXP_NHE and EXP_CTL (i.e., EXP_NHE minus EXP_CTL).
 297 Stippling in (c) and (d) denote differences statistically significant at the 95% confidence
 298 level.

299

300 *b. Quantitative evaluation of forecast skills*

301 For medium-range forecast, the wind circulation in the troposphere is often of
 302 greater interest than in the stratosphere. To better evaluate the performance of the
 303 revised OGWD scheme, Figures 3a and 3b depict the mean bias (MB) and root mean
 304 square error (RMSE) for the 500 hPa geopotential height (GPH500) in the two
 305 experiments. Herein, we are interested in the NH because of the relatively weak wind
 306 differences in the SH (Fig. 1d) which is mainly covered by the ocean. Moreover, as will
 307 be shown below, the parameterized OGWD changes little in the SH.

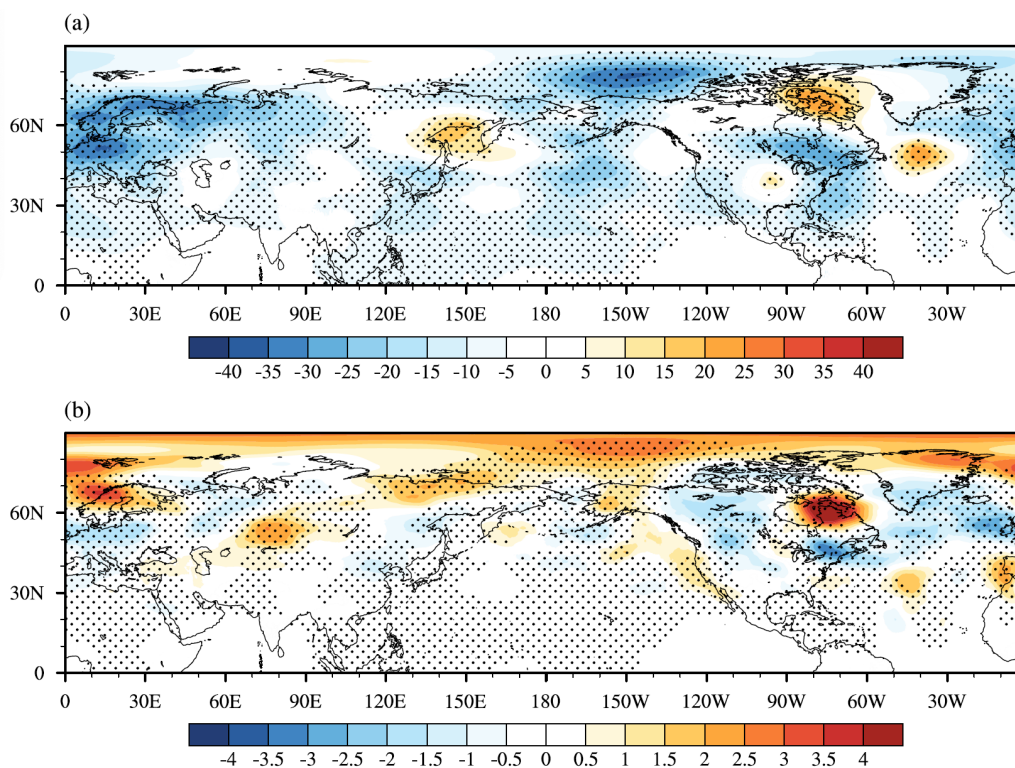


308

309 Figure 3. (a) Mean bias and (c) RMSE of the GPH500 in the NH at different forecast
310 lead time. (b) and (d) are similar to (a) and (c) but in the region north of 60°N.

311

312 In both experiments, the model GPH500 is lower than the ERA5 reanalysis, with
313 the MB and RMSE increasing with the forecast lead time (Figs. 3a, 3c). The GPH500
314 shows obvious underestimation in the EXP_CTL experiment which are significantly
315 reduced in EXP_NHE. This improvement is particularly evident in high latitudes north
316 of 60°N which is overall statistically significant at the 95% confidence level (Figs. 4a,
317 4b). Compared to EXP_CTL, EXP_NHE exhibits even greater MB and RMSE of
318 GPH500 till the 6th forecast day. Nevertheless, both the MB and RMSE of the GPH500
319 decrease quickly afterwards, which are reduced by 11.59% and 5.06%, respectively, at
320 the 10th day of the forecast (Table 1). Greater improvements are found for the GPH500
321 between 60°N and 90°N, the MB and RMSE of which are decreased by 31.18% and
322 15.93%, respectively, at the 10th forecast day (Table 1). All the values shown in Table
323 1 are statistically significant at the 95% confidence level. For the total 10 forecast days
324 as a whole, the MB and RMSE of GPH500 are separately reduced by 2.6% and 0.52 %,
325 indicating an overall improvement in the simulation of the large-scale circulation in the
326 NH when using the revised OGWD scheme (see Table 2).



327

328 Figure 4. (a) Mean biases of GPH500 (shading; units: gpm) in EXP_CTL experiment
 329 as compared to ERA5 averaged over the ten forecast days. (b) is similar to (a) but for
 330 the differences between the GPH500 (shading; units: gpm) in EXP_CTL and
 331 EXP_NHE experiments (i.e., EXP_NHE minus EXP_CTL). Stippling in (a) and (b)
 332 denote differences statistically significant at the 95% confidence level.

333

334 Table 1. Mean bias and RMSE of the 500-hPa geopotential height (GPH500) and sea
 335 level pressure (SLP) at the 10th forecast day

	Region	Mean Bias			RMSE		
		CTL	NHE	$\frac{NHE - CTL}{CTL} \times 100$	CTL	NHE	$\frac{NHE - CTL}{CTL} \times 100$
GPH500 (gpm)	0-90°N	-12.825	-11.338	-11.59	25.263	23.984	-5.06
	60°N-90°N	-16.841	-11.590	-31.18	28.017	23.554	-15.93
SLP (hPa)	0-90°N	-0.522	-0.343	-34.29	2.714	2.515	-8.33
	60°N-90°N	-1.712	-1.079	-36.97	3.049	2.517	-17.45

336

337 Table 2. Mean bias and RMSE of the 500-hPa geopotential height (GPH500) and sea
 338 level pressure (SLP) for the overall ten forecast days

		Mean Bias			RMSE		
	Region	CTL	NHE	$\frac{NHE - CTL}{CTL} \times 100$	CTL	NHE	$\frac{NHE - CTL}{CTL} \times 100$
GPH500 (gpm)	0-90°N	-7.923	-7.717	-2.6	16.455	16.369	-0.52
	60°N-90°N	-9.187	-8.438	-8.15	16.470	16.089	-2.31
SLP (hPa)	0-90°N	-0.107	-0.082	-23.46	1.87	1.841	-1.53
	60°N-90°N	-0.498	-0.411	-17.47	1.598	1.532	-4.13

339

340 Besides the GPH500, the forecast skill is also examined for the SLP in the NH.

341 As shown in Fig. 5a, the EXP_CTL experiment systematically underestimates the SLP

342 over East Asia and the Arctic, while overestimating SLP across North America and the

343 northern Atlantic. These biases are substantially corrected in the EXP_NHE experiment,

344 particularly in high-latitude regions north of 60°N (Fig. 5b). Similarly, the EXP_NHE

345 experiment firstly experiences a degradation in the early 6 days compared to EXP_CTL,

346 but it shows significant improvement at the end of the 10th forecast day, with the MB

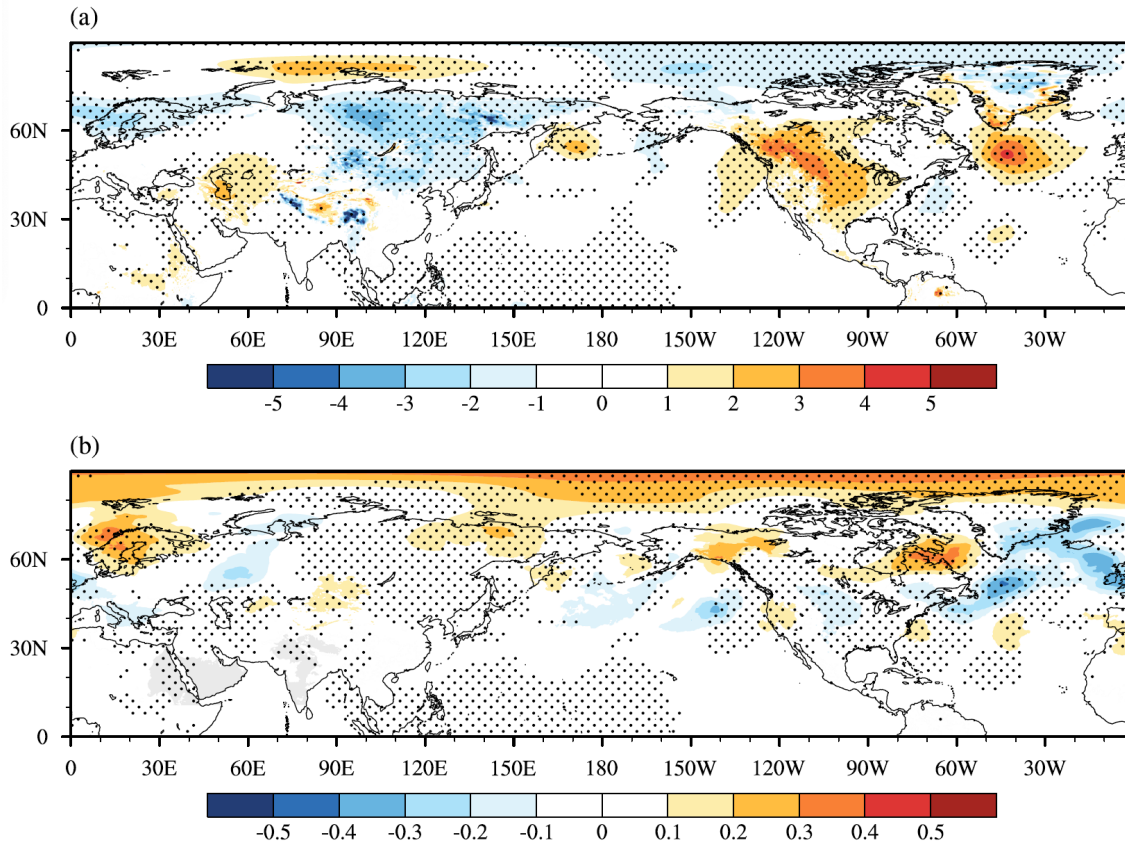
347 reduced by 34.29% and the RMSE by 8.33%, respectively (Table 1). Greater decreases

348 of 36.97% (for MB) and 17.45% (for RMSE) are found in the high latitudes north of

349 60°N as well.

350

351



352

353 Figure 5. (a) Mean biases of SLP (shading; units: hPa) in the EXP_CTL experiment as
 354 compared to ERA5 averaged over the ten forecast days. (b) is similar to (a) but for the
 355 differences between the SLP (shading; units: hPa) in the EXP_CTL and EXP_NHE
 356 experiments (i.e., EXP_NHE minus EXP_CTL). Stippling in (a) and (b) denote
 357 differences statistically significant at the 95% confidence level.

358

359 From the above analyses, implementing the revised OGWD scheme in the high-
 360 resolution CMA-GFS model can help improve the medium range forecast of the NH
 361 large-scale circulation, especially in the high latitudes. In the next section, we will
 362 examine the underlying mechanisms responsible for the improvement of the circulation.

363

364

365 4. Physical interpretation

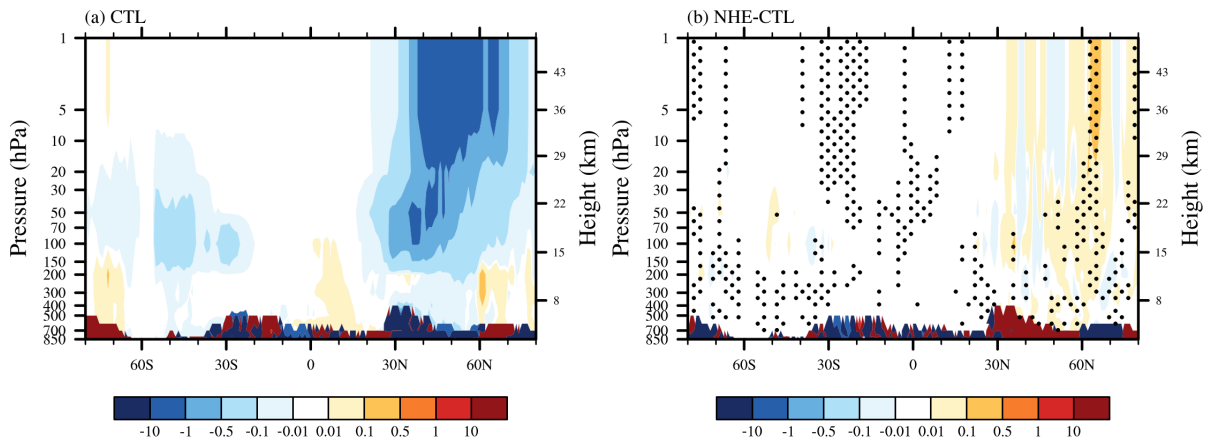
366 a. Changes of parameterized OGWD

367 The changes of wind circulation arise from the revision of the OGWD scheme.
368 It is thus straightforward to study the parameterized OGWD in these two experiments.
369 Figure 6a shows the vertical distribution of zonal-mean zonal OGWD averaged in the
370 period of 10 December 2023 to 10 January 2024 in the EXP_CTL experiment. The
371 differences between the parameterized OGWD in the two experiments (i.e., EXP_NHE
372 minus EXP_CTL) are given in Fig. 6b. In boreal winter, there exists prominent OGWD
373 in the stratosphere of the NH mid-to-high latitudes, which is favored by the decrease of
374 air density with height (e.g., Lindzen, 1981) and the relatively weak winds between the
375 tropospheric jet and polar night jet. The latter is called as the “valve layer” by Kruse et
376 al. (2016). The maximum OGWD occurs between about 20 hPa and 1 hPa. In contrast,
377 there is very weak OGWD in the SH stratosphere owing to the critical level absorption
378 as mentioned above.

379 Compared to that in EXP_CTL, the zonal-mean zonal OGWD in EXP_NHE is
380 generally weakened in the high latitudes of the NH (north of about 55°N), especially in
381 the stratosphere (Fig. 6b). Note that the positive difference indicates a decrease of
382 OGWD as the drag itself is negative. This is due to the fact that the NHE acts to decrease
383 the surface WMF [see Eqs. (4) and (5)], i.e., the source of parameterized OGWs which
384 determines the maximum wave momentum that can be deposited into the mean flow.
385 Therefore, the decrease of surface WMF is prone to reduce the OGWD. Note that there
386 is also enhancement of OGWD, e.g., in the stratosphere near 50°N. This may be
387 attributed to a decrease in surface WMF, which suppresses tropospheric wave breaking

388 by lowering the gravity-wave amplitude limit for breaking at lower levels and thus
 389 shifts the wave-breaking altitude upward. Consequently, a vertical structure
 390 characterized by alternating positive-negative-positive anomalies from the surface to
 391 the stratosphere would be expected. In consequence, more WMF is transported to the
 392 stratosphere where the OGWs break owing to the decay of air density and lead to
 393 stronger OGWD. This is similar to the redistribution of WMF in the vertical owing to
 394 selective critical level filtering of OGWs in directional shear flows (Shutts, 1995; Xu
 395 et al., 2012, 2019; van Niekerk et al., 2023). Generally, the changes in the vertical
 396 structure of parameterized OGWD in the CMA-GFS model are similar to that in the
 397 MPAS seasonal simulations conducted in Xu et al. (2024) which also considers the
 398 NHE correction to the OGWD (cf. their Fig. 5).

399



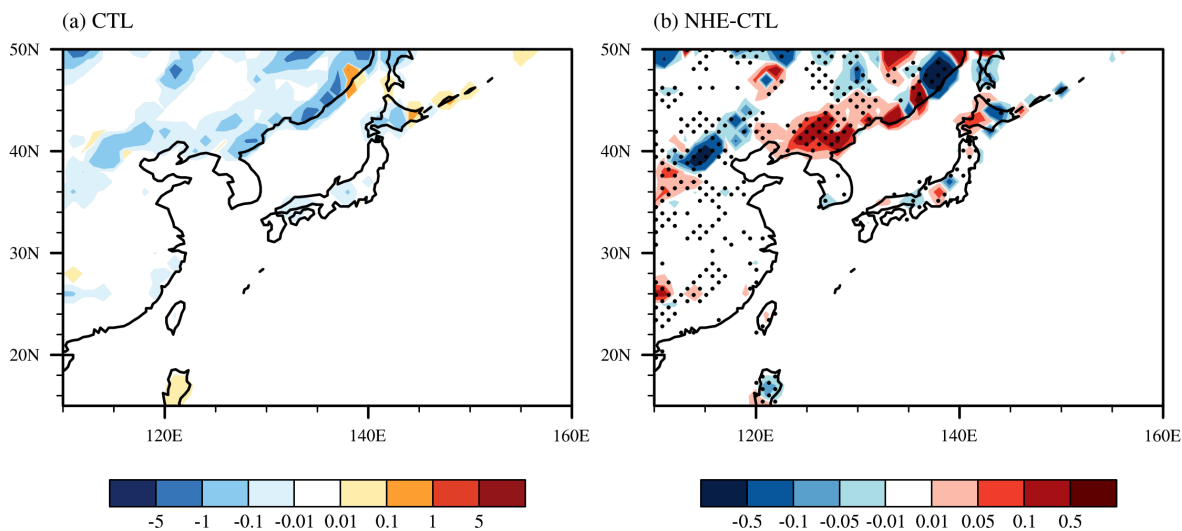
400

401 Figure 6. Vertical distributions of (a) zonal-mean zonal OGWD (units: $\text{m s}^{-1} \text{ day}^{-1}$)
 402 averaged in the period of 10 December 2023 to 10 January 2024 obtained from
 403 EXP_CTL, and (b) zonal-mean OGWD difference between the two experiments of
 404 EXP_NHE and EXP_CTL (i.e., EXP_NHE minus EXP_CTL). Stippling in (b) denotes
 405 differences statistically significant at the 95% confidence level.

406

407 The weakening of OGWD can directly increase the zonal winds in the polar
 408 stratosphere and the mid-latitude troposphere of the NH, thus leading to a recover of
 409 the weakened westerly jet. Conversely, the enhancement of OGWD can directly weaken
 410 the zonal winds in the mid-latitude stratosphere and the polar troposphere of the NH,
 411 thereby reducing the westerly biases (Figs. 1c, 1d). The parameterized OGWD in East
 412 Asia is also examined to explain the changes of EASJ. As shown in Fig. 7a, there is
 413 notable westward OGWD at 200 hPa in the high latitudes of East Asia where the
 414 underlying terrain is very complex, such as the Taihang, Yanshan, Changbai, Greater
 415 Khingan and Lesser Khingan Mountains. Thus, the largest easterly biases of the EASJ
 416 occur in this region (Fig. 2c). When accounting for the NHE in the OGWD
 417 parameterization scheme, the 200-hPa OGWD is mainly reduced (Fig. 7b). Clearly, the
 418 enhanced EASJ is owing to the weakening of the parameterized OGWD.

419



420
 421 Figure 7. Horizontal distributions of (a) zonal OGWD (units: $\text{m s}^{-1} \text{ day}^{-1}$) at 200 hPa
 422 averaged in the period of 10 December 2023 to 10 January 2024 obtained from
 423 EXP_CTL, and (b) zonal OGWD difference between the two experiments of EXP_NHE

424 and EXP_CTL (i.e., EXP_NHE minus EXP_CTL) at 200 hPa. Stippling in (b) denotes
425 differences statistically significant at the 95% confidence level.

426

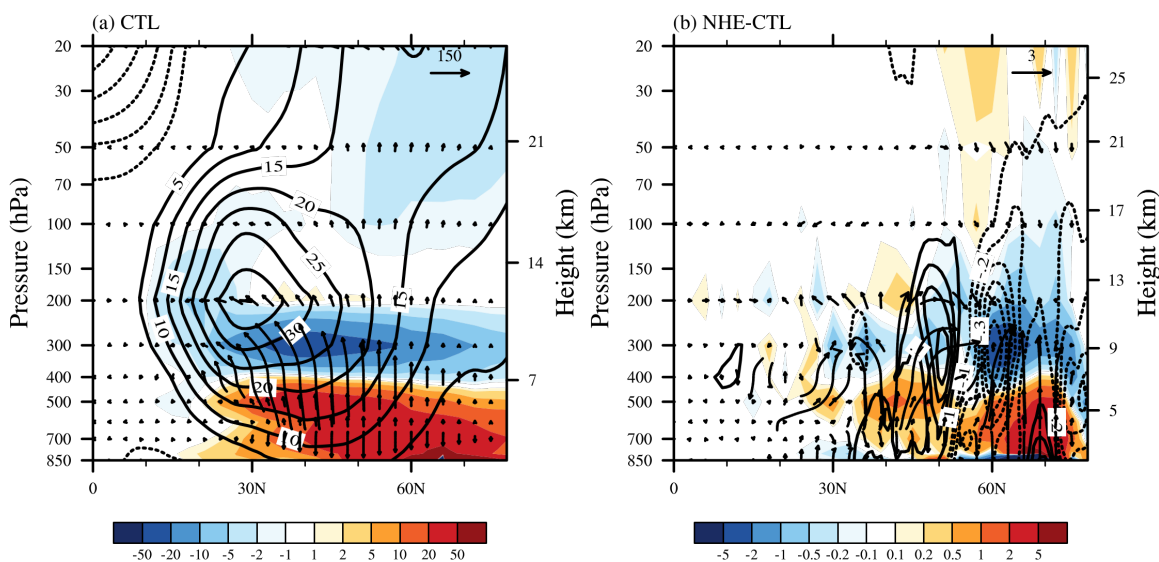
427 *b. Resolved Rossby-wave adjustment*

428 In addition to the direct effect of the modified OGWD, the tropospheric response
429 in the Northern Hemisphere is also associated with an adjustment of resolved large-scale
430 Rossby waves. This interpretation is consistent with the wave-drag compensation and
431 propagation-adjustment mechanisms discussed in previous studies (e.g., Cohen et al., 2013;
432 Sigmund and Shepherd, 2014). In particular, changes in the background zonal wind may
433 alter the propagation conditions for planetary waves and thereby redistribute the resolved
434 wave forcing between the troposphere and stratosphere.

435 It is well known that the impacts of large-scale Rossby waves on the mean flow
436 can be measured by the convergence of the zonal-mean Eliassen-Palm (EP) flux. Figure
437 8a illustrates the distribution of the zonal-mean EP flux in the EXP_CTL experiment
438 which is calculated following Edmon et al. (1980). In the NH middle-to-high latitudes,
439 Rossby waves originate from the lower troposphere which propagate upward and
440 converge in the upper troposphere. These waves split into two branches in the lower
441 stratosphere. The first branch turns to propagate equatorward across the tropospheric
442 jet. The other branch continues to propagate upward to the upper stratosphere where
443 the EP flux is converged and decelerates the mean flow. As in the SH, the Rossby waves
444 cannot propagate into the stratosphere (not shown) because of the presence of easterlies
445 there during austral summer (Fig. 1a).

446 Figure 8b is similar to Fig. 8a but gives the differences between the zonal-mean
447 EP fluxes in the two experiments (i.e., EXP_NHE minus EXP_CTL). Compared to

448 EXP_CTL, the upward propagation of Rossby waves into the stratosphere is suppressed
 449 in the high latitudes of the NH, leading to an enhanced convergence of EP flux in the
 450 troposphere. As a result, the zonal-mean zonal winds in the NH polar troposphere are
 451 decelerated by the large-scale Rossby wave forcing, which contributes to the alleviation
 452 of westerly biases there (Figs. 1c, 1d). This may explain why the improvements in the
 453 GPH 500 forecast emerge after 6 days in EXP_NHE (Fig. 2). The Rossby waves and
 454 their interaction with the mean flow require several days to develop fully and influence
 455 the large-scale circulation.
 456



457
 458 Figure 8. Vertical distributions of zonal-mean EP flux (vectors) and its divergence
 459 (shading; $\text{m s}^{-1} \text{ day}^{-1}$) due to resolved waves averaged in the period of 10 December
 460 2023 to 10 January 2024 obtained from (a) EXP_CTL, and (b) the difference between
 461 the two experiments of EXP_NHE and EXP_CTL (i.e., EXP_NHE minus EXP_CTL).
 462 Contours are the corresponding zonal-mean zonal wind (units: m s^{-1}).
 463

464 The suppressed upward propagation of Rossby waves can be understood from
 465 the changes of the refractive index (*RFI*) that measures the ability of Rossby wave
 466 propagation (e.g., Chen and Robinson, 1992; Hu et al., 2019), which is defined as

$$467 \quad RFI = \left[\frac{\overline{q_\varphi}}{r\overline{U}} - \left(\frac{k}{r\cos\varphi} \right)^2 - \left(\frac{f}{2NH} \right)^2 \right] r^2, \quad (6)$$

468 where \overline{U} , k and H are the resolved zonal-mean zonal wind, zonal wave number and density
 469 scale height, respectively. $\overline{q_\varphi}$ represents the meridional gradient of the potential vorticity,
 470 which is expressed in the following form of

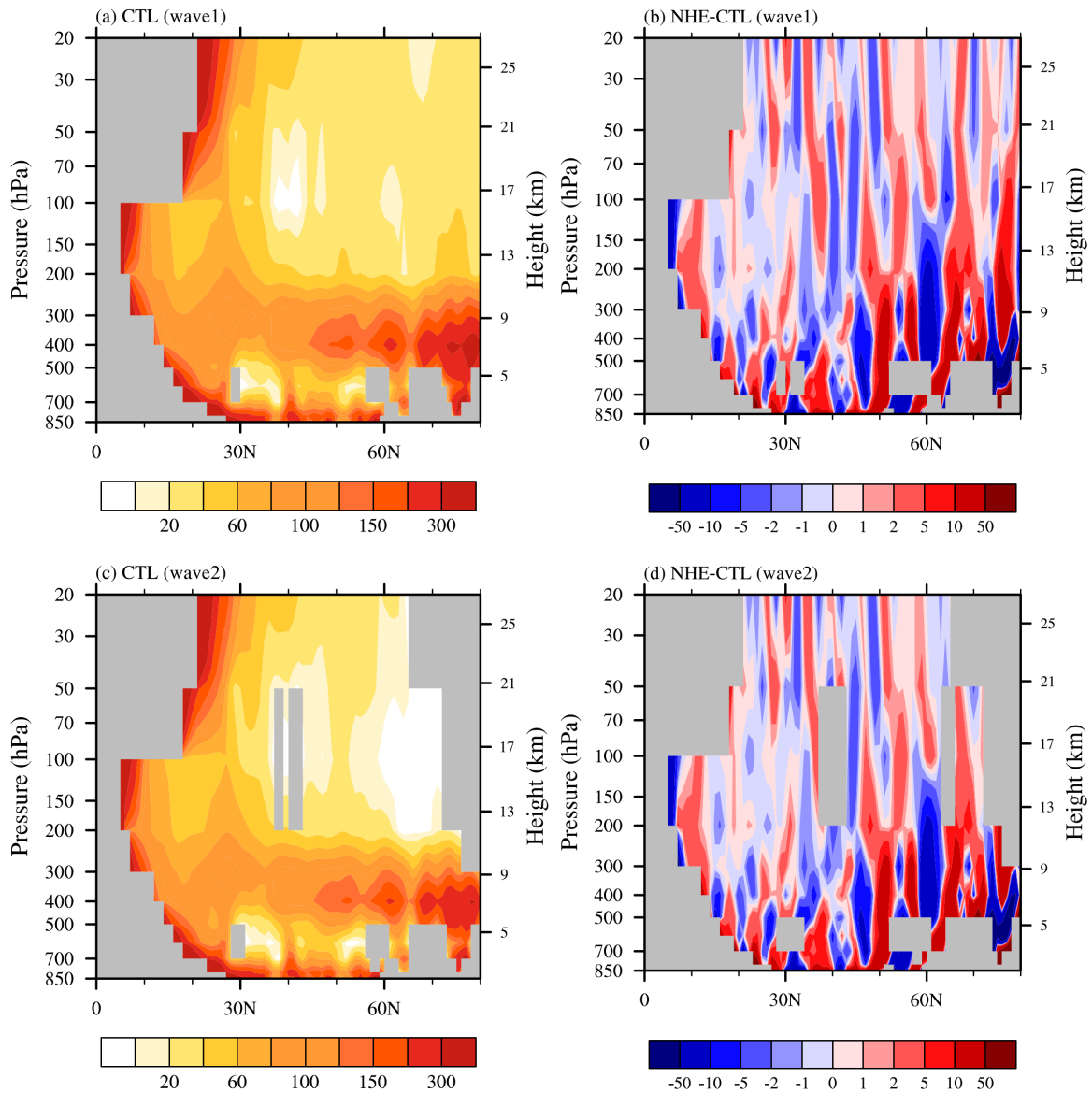
$$471 \quad \overline{q_\varphi} = 2\Omega\cos\varphi - \left[\frac{(\overline{U}\cos\varphi)_\varphi}{a\cos\varphi} \right]_\varphi + \frac{af^2}{R_d} \left(\frac{p\theta}{T} \frac{\overline{U}_p}{\theta_p} \right)_p. \quad (7)$$

472 where Ω , θ and R_d being the Earth's angular frequency, potential temperature and
 473 dry gas constant, respectively. The subscripts φ and p represent the partial derivatives with
 474 respect to latitude and pressure, respectively. The overbars indicate temporal and zonal
 475 averages. From Eq. (6), the increase of zonal wind will narrow the range of Rossby
 476 wave numbers that can propagate into the stratosphere (Charney and Drazin, 1961; Xu
 477 et al., 2024).

478 As shown in Fig. 9, positive *RFI* values for both zonal wavenumbers 1 and 2 are
 479 found over the northern mid- to high latitudes in EXP_CTL, indicating that the basic-
 480 state flow is favorable for the upward propagation of planetary waves (Figs. 9a, 9c).
 481 In EXP_NHE, however, the *RFI* is generally reduced over the same region, especially
 482 in the upper troposphere and lower stratosphere. These negative *RFI* anomalies suggest
 483 that the strengthened background westerlies in the polar stratosphere make the

484 environment less conducive to the vertical propagation of Rossby waves (Figs. 9b, 9d).
485 Similar behavior is found for both wavenumber-1 and wavenumber-2 components,
486 although the wavenumber-1 signal appears more spatially coherent. Therefore, the
487 reduction of *RFI* provides a dynamical explanation for the weakened upward EP-flux
488 branch seen in Fig. 8b.

489 Physically, the revised OGWD scheme weakens the parameterized drag in the
490 northern polar stratosphere, which strengthens the local westerlies. Stronger
491 background westerlies narrow the range of planetary-wave numbers that can propagate
492 vertically into the stratosphere. Consequently, the upward propagation of resolved
493 Rossby waves is suppressed, and less resolved wave forcing reaches the polar
494 stratosphere. This effect acts together with the weakened parameterized OGWD to
495 reduce the easterly wind bias in the polar stratosphere. At the same time, the associated
496 redistribution of resolved wave forcing favors a weakening of the polar-tropospheric
497 westerlies, thereby contributing to the improvement of the large-scale circulation over
498 the northern high latitudes.



499

500 Figure 9. Refractive index for the (a) wavenumber-1 and (c) wavenumber-2 resolved
 501 waves averaged over the period of 10 December 2023 to 10 January 2024 in the
 502 EXP_CTL experiment. (b) The difference between the refractive indices of
 503 wavenumber 1 in EXP_NHE and EXP_CTL (EXP_NHE minus EXP_CTL). (d) As in
 504 (b), but for wavenumber 2.

505

506 **4. Summary and discussions**

507 The latest China Meteorological Administration Global Forecast System (CMA-
508 GFS) v4.0 model has been upgraded to a higher resolution of 0.125° in 2023. However,
509 this high-resolution global model still uses the parameterization scheme of orographic
510 gravity wave drag (OGWD) developed by Kim and Arakawa (1995; KA95) which is
511 based on hydrostatic orographic gravity wave (OGW) theory. In this study, the KA95
512 OGWD scheme is revised by taking into account the nonhydrostatic effect (NHE) on
513 the surface wave momentum flux (WMF) of OGWs, according to the nonhydrostatic
514 OGW theory derived in our earlier study of Xu et al. (2021). The performance of the
515 revised OGWD scheme is then evaluated for the medium-range forecast of the CMA-
516 GFSv4.0 model. Two sets of numerical experiments (i.e., EXP_CTL and EXP_NHE)
517 are conducted by using the original KA95 scheme and the revised NHE scheme,
518 respectively. In each numerical experiment, there are in total 31 forecasts of 10-day
519 forecasts. [In each numerical experiment, there are in total 31 independent 10-day](#)
520 [forecasts which are initiated at 00 UTC on each day of December 2023.](#)

521 The results show that the revised OGWD scheme can improve the medium-
522 range forecast of large-scale circulation in the Northern Hemisphere (NH), especially
523 in the high latitudes. The easterly biases of zonal-mean zonal wind in the NH
524 stratosphere are reduced, with both the magnitude and location of the polar night jet
525 being better captured. The underestimation of the East Asia subtropical jet (EASJ) is
526 also alleviated. In contrast, the revised OGWD scheme shows little influence on the
527 stratospheric circulation in the Southern Hemisphere (SH). This is because, in boreal
528 winter (i.e., austral summer), there is hardly OGWD in the SH stratosphere owing to
529 the effect of critical-level absorption, [leading to comparatively smaller circulation](#)

530 responses. Therefore, the quantitative evaluation of forecast skill is mainly performed
531 for the NH, where the impact of the revised OGWD scheme is physically more
532 pronounced and statistically more robust.

533 Quantitative evaluation is performed for the medium-range forecast skills in the
534 NH, taking the ERA5 reanalysis dataset as reference. Both experiments showed lower
535 geopotential height (GPH) at 500 hPa than ERA5 reanalysis, with the mean bias (MB)
536 and root mean square error (RMSE) increasing with forecast lead time. EXP_NHE
537 initially has greater MB and RMSE than EXP_CTL until the 6th forecast day, but these
538 metrics decrease more rapidly afterwards, resulting in an 11.59% reduction in MB and
539 a 5.06% reduction in RMSE by day 10. Over the total 10 forecast days, the MB and
540 RMSE of the GPH 500 in the NH are reduced by 2.6% and 0.52%, respectively,
541 indicating improved simulation of large-scale circulation in the NH. The improvement
542 is more noticeable in the high latitudes north of about 60°N, where the MB and RMSE
543 of GPH 500 are decreased by 31.18% and 15.93% at the 10th forecast day. Similar
544 results are found for the sea level pressure (SLP) in the NH, the MB and RMSE of
545 which are reduced by 34.29% and 8.33%, respectively, by day 10 in EXP_NHE.

546 The dynamics responsible for the improvement of large-scale wind circulation are
547 examined. The NHEs act to decrease the surface WMF of OGWs, which leads to a general
548 weakening of the parameterized OGWD in the midlatitudes and high latitudes of the NH.
549 This weakening of OGWD directly increases the zonal winds in the mid-latitude
550 troposphere and polar stratosphere, reducing the easterly biases. The enhanced zonal wind
551 in the polar stratosphere acts to narrow the range of large-scale Rossby wave numbers
552 that can propagate into the stratosphere by reducing the refractive index of Rossby waves.

553 The suppressed upward propagation of Rossby waves leads to greater convergence of
554 Eliassen-Palm (EP) flux (i.e., resolved wave forcing) in the NH polar troposphere, which
555 decelerates the zonal winds and thus alleviates the westerly biases there.

556 To sum up, this study demonstrates that incorporating the NHE into the OGWD
557 parameterization scheme can help improve the simulation of large-scale atmospheric
558 circulation in high-resolution global NWP models, which is thus important for accurate
559 weather forecasts and/or climate simulations. However, there are still some limitations in
560 this work. For example, this study pays much attention to the medium-range forecast of
561 large-scale circulation in winter of NH. To further validate its effectiveness and robustness,
562 it is necessary to conduct more comprehensive evaluations of the nonhydrostatic OGWD
563 scheme in various numerical models focusing on different weather and climate systems.
564 Additionally, this work only takes into account the effects of NHE on the OGWD. Other
565 factors such as the vertical wind shear could also greatly affect the OGWD (e.g., Xu et al.,
566 2019; Xu et al., 2020; Zhang et al., 2025). While Xu et al. (2021) explored the
567 nonhydrostatic OGWs generated in a constant flow, it remains unclear how the vertical
568 wind shear affects the behavior of nonhydrostatic OGWs which needs further study.

569

570 *Code and data availability.* The China Meteorological Administration Global Forecast
571 System (CMA-GFS) model is archived on Zenodo under
572 <https://doi.org/10.5281/zenodo.18476721> (Zhang, 2026). The CMA-GFS outputs and the
573 ERA5 reanalysis data used for the comparison, along with the codes for orographic gravity
574 wave scheme are uploaded to <https://doi.org/10.5281/zenodo.18529537> (Zhang, 2026).

575

576 *Author contributions.* RRZ was responsible for formal analysis, writing the original draft
577 and visualization. ZZA carried out data analyses. XX developed the code and conducted
578 the analysis. HLX and QYC provided the resources and data curation.

579

580 *Competing interests.* The contact author has declared that none of the authors has any
581 competing interests.

582

583 *Acknowledgements.* The authors would like to express their sincere thanks to the
584 anonymous referees.

585

586 *Financial support.* This work is mainly supported by the National Natural Science
587 Foundation of China (grants no. U2342226, 42275163), the Joint Research Project for
588 Meteorological Capacity Improvement (grant no. 22NLTSZ006), and Jiangsu
589 Meteorological Observatory (grant no. KQ202502).

590

591

592 **References**

- 593 Alexander, M. J., Geller, M., McLandress, C., Polavarapu, S., Preusse, P., Sassi, F., Sato,
594 K., Eckermann, S., Ern, M., Hertzog, A., Kawatani, Y., Pulido, M., Shaw, T.A.,
595 Sigmond, M., Vincent, R. and Watanabe, S.: Recent developments in gravity-wave
596 effects in climate models and the global distribution of gravity-wave momentum
597 flux from observations and models, *Quarterly Journal of the Royal Meteorological*
598 *Society*, 136, 1103-1124, <https://doi.org/10.1002/qj.637>, 2010.
- 599 Alpert, J.: Sub-grid scale mountain blocking at NCEP, 20th Conference on Weather
600 Analysis and Forecasting/16th Conference on Numerical Weather Prediction,
601 https://ams.confex.com/ams/84Annual/techprogram/program_185.htm, 2004.
- 602 Beljaars, A. C. M., Brown, A. R., and Wood, N.: A new parametrization of turbulent
603 orographic form drag, *Quarterly Journal of the Royal Meteorological Society*, 130,
604 1327-1347, <https://doi.org/10.1256/qj.03.73>, 2004.
- 605 Booker, J. R., and Bretherton, F. P.: The critical layer for internal gravity waves in a shear
606 flow, *Journal of Fluid Mechanics*, 27, 513-539,
607 <https://doi.org/10.1017/S0022112067000515>, 1967.
- 608 Charney, J. G., and Drazin, P. G.: Propagation of planetary-scale disturbances from the
609 lower into the upper atmosphere, *Journal of Geophysical Research (1896-1977)*, 66,
610 83-109, <https://doi.org/10.1029/JZ066i001p00083>, 1961.
- 611 Chen, J., Ma, Z., Li, Z., Shen, X., Su, Y., Chen, Q., and Liu, Y.: Vertical diffusion and
612 cloud scheme coupling to the Charney-Phillips vertical grid in GRAPES global
613 forecast system, *Quarterly Journal of the Royal Meteorological Society*, 146, 2191-
614 2204, <https://doi.org/10.1002/qj.3787>, 2020.

- 615 Chen Q., Shen, X., Sun, J., and Liu, K.: Momentum budget diagnosis and the
616 parameterization of subgrid-scale orographic drag in global GRAPES, *Journal of*
617 *Meteorological Research*, 30, 771-788, <https://doi.org/10.1007/s13351-016-6033->
618 [y](https://doi.org/10.1007/s13351-016-6033-y), 2016.
- 619 Chen, P., and Robinson, W. A.: Propagation of Planetary Waves between the Troposphere
620 and Stratosphere, *Journal of Atmospheric Sciences*, 49, 2533-2545,
621 [https://doi.org/10.1175/1520-0469\(1992\)049<2533:POPWBT>2.0.CO;2](https://doi.org/10.1175/1520-0469(1992)049<2533:POPWBT>2.0.CO;2), 1992.
- 622 Choi, H. J., and Hong, S. Y.: An updated subgrid orographic parameterization for global
623 atmospheric forecast models, *Journal of Geophysical Research: Atmospheres*, 120,
624 12445-12457, <https://doi.org/10.1002/2015JD024230>, 2015.
- 625 Cohen, N. Y., Gerber, E. P., and Buhler, O.: Compensation between resolved and
626 unresolved wave driving in the stratosphere: Implications for downward control,
627 *Journal of the Atmospheric Sciences*, 70, 3780-3798, <https://doi.org/10.1175/JAS->
628 [D-12-0346.1](https://doi.org/10.1175/JAS-D-12-0346.1), 2013.
- 629 Dai, Y., Zeng, X., Robert, E. D., Baker, L., Bonan, G. B., Bosilovich, M. G., Denning A.
630 S., Dirmeyer, P. A., Houser, P. R., Niu, G., Oleson, K. W., Schlosser, C. A., Yang,
631 Z.: The Common Land Model, *Bulletin of the American Meteorological Society*,
632 84, 1013-1024, <https://doi.org/10.1175/BAMS-84-8-1013>, 2003.
- 633 Edmon, H. J., Hoskins, B. J. and McIntyre, M. E.: Eliassen-Palm Cross Sections for the
634 Troposphere, *Journal of Atmospheric Sciences*, 37, 2600-2616,
635 [https://doi.org/10.1175/1520-0469\(1980\)037<2600:EPCSFT>2.0.CO;2](https://doi.org/10.1175/1520-0469(1980)037<2600:EPCSFT>2.0.CO;2), 1980.

- 636 Fritts, D. C., and Alexander, M. J.: Gravity wave dynamics and effects in the middle
637 atmosphere, *Reviews of Geophysics*, 41, <https://doi.org/10.1029/2001RG000106>,
638 2003.
- 639 Han, J., and Pan, H. L.: Revision of Convection and Vertical Diffusion Schemes in the
640 NCEP Global Forecast System, *Weather and Forecasting*, 26, 520-533,
641 <https://doi.org/10.1175/WAF-D-10-05038.1>, 2011.
- 642 Haynes, P. H., McIntyre, M. E., Shepherd, T. G., Marks, C. J., and Shine, K. P.: On the
643 “Downward Control” of Extratropical Diabatic Circulations by Eddy-Induced
644 Mean Zonal Forces, *Journal of Atmospheric Sciences*, 48, 651-678,
645 [https://doi.org/10.1175/1520-0469\(1991\)048<0651:OTCOED>2.0.CO;2](https://doi.org/10.1175/1520-0469(1991)048<0651:OTCOED>2.0.CO;2), 1991.
- 646 Hersbach, H., Bell, B., Berrisford, P., et al: The ERA5 global reanalysis, *Quarterly Journal*
647 *of the Royal Meteorological Society*, 146, 1999-2049,
648 <https://doi.org/10.1002/qj.3803>, 2020.
- 649 Hong, S. Y., and Pan, H. L.: Nonlocal Boundary Layer Vertical Diffusion in a Medium-
650 Range Forecast Model, *Monthly Weather Review*, 124, 2322-2339,
651 [https://doi.org/10.1175/1520-0493\(1996\)124<2322:NBLVDI>2.0.CO;2](https://doi.org/10.1175/1520-0493(1996)124<2322:NBLVDI>2.0.CO;2), 1996.
- 652 Hu, D., Guo, Y., and Guan, Z.: Recent Weakening in the Stratospheric Planetary Wave
653 Intensity in Early Winter, *Geophysical Research Letters*, 46, 3953-3962,
654 <https://doi.org/10.1029/2019GL082113>, 2019.
- 655 Kim, Y. J.: Balance of drag between the middle and lower atmospheres in a global
656 atmospheric forecast model, *Journal of Geophysical Research: Atmospheres*, 112,
657 <https://doi.org/10.1029/2007JD008647>, 2007.

- 658 Kim, Y. J., and Arakawa, A.: Improvement of Orographic Gravity Wave Parameterization
659 Using a Mesoscale Gravity Wave Model, *Journal of Atmospheric Sciences*, 52,
660 1875-1902, [https://doi.org/10.1175/1520-
661 0469\(1995\)052<1875:IOOGWP>2.0.CO;2](https://doi.org/10.1175/1520-0469(1995)052<1875:IOOGWP>2.0.CO;2), 1995.
- 662 Kim, Y. J., and Doyle, J. D.: Extension of an orographic-drag parametrization scheme to
663 incorporate orographic anisotropy and flow blocking, *Quarterly Journal of the
664 Royal Meteorological Society*, 131, 1893-1921, <https://doi.org/10.1256/qj.04.160>,
665 2005.
- 666 Kim, Y. J., Eckermann, S., and Chun, H. Y.: An overview of the past, present and future
667 of gravity-wave drag parametrization for numerical climate and weather prediction
668 models - Survey article, *Atmosphere-ocean*, 41, 65-98,
669 <https://doi.org/10.3137/ao.410105>, 2003.
- 670 Klemp, J. B., and Durran, D. R.: An Upper Boundary Condition Permitting Internal Gravity
671 Wave Radiation in Numerical Mesoscale Models, *Monthly Weather Review*, 111,
672 430-444, [https://doi.org/10.1175/1520-0493\(1983\)111<0430:AUBCPI>2.0.CO;2](https://doi.org/10.1175/1520-0493(1983)111<0430:AUBCPI>2.0.CO;2),
673 1983.
- 674 Kruse, C. G., Smith, R. B., and Eckermann, S. D.: The Midlatitude Lower-Stratospheric
675 Mountain Wave “Valve Layer”, *Journal of the Atmospheric Sciences*, 73, 5081-
676 5100, <https://doi.org/10.1175/JAS-D-16-0173.1>, 2016.
- 677 Li, M., Xu, X., Teixeira, M. A. C., Xue, M., Xue, H., Zhu, K., and Huang, H.: Improved
678 Orographic Gravity Wave Drag Parameterization Accounting for the
679 Nonhydrostatic Effect in the Weather Research and Forecasting Model: Tests for

- 680 Short-Range Forecast of Northeast China Cold Vortices, *Monthly Weather Review*,
681 152, 2623-2637, <https://doi.org/10.1175/MWR-D-24-0097.1>, 2024.
- 682 Li, R., Xu, X., Xu, X., Shepherd, T. G., and Wang, Y.: Importance of orographic gravity
683 waves over the Tibetan Plateau on the spring rainfall in East Asia, *Science China
684 Earth Sciences*, 66, 2594-2602, <https://doi.org/10.1007/s11430-023-1204-6>, 2023.
- 685 Lindzen, R. S.: Turbulence and stress owing to gravity wave and tidal breakdown, *Journal
686 of Geophysical Research: Oceans*, 86, 9707-9714,
687 <https://doi.org/10.1029/JC086iC10p09707>, 1981.
- 688 Liu, K., Chen, Q., and Sun, J.: Modification of cumulus convection and planetary boundary
689 layer schemes in the GRAPES global model, *Journal of Meteorological Research*,
690 29, 806-822, <https://doi.org/10.1007/s13351-015-5043-5>, 2015.
- 691 Lott, F., and Miller, M. J.: A new subgrid-scale orographic drag parametrization: Its
692 formulation and testing, *Quarterly Journal of the Royal Meteorological Society*,
693 123, 101-127, <https://doi.org/10.1002/qj.49712353704>, 1997.
- 694 Lu, Y., Wu, T., Xu, X., Zhang, L., and Chu, M.: Improved Simulation of the Antarctic
695 Stratospheric Final Warming by Modifying the Orographic Gravity Wave
696 Parameterization in the Beijing Climate Center Atmospheric General Circulation
697 Model, *Atmosphere*, 11, 576, <https://doi.org/10.3390/atmos11060576>, 2020.
- 698 Lu, Y., Xu, X., Wang, L., Liu, Y., Wu, T., Jie, W., and Sun, J.: Machine Learning
699 Emulation of Subgrid-Scale Orographic Gravity Wave Drag in a General
700 Circulation Model with Middle Atmosphere Extension, *J. Adv. Model. Earth Syst.*,
701 16, e2023MS003611, <https://doi.org/10.1029/2023MS003611>, 2024.

- 702 Ma, Z., Liu, Q., Zhao, C., Shen, X., Wang, Y., Jiang, J. H., Zhe, L., and Yung, Y.:
703 Application and Evaluation of an Explicit Prognostic Cloud-Cover Scheme in
704 GRAPES Global Forecast System, *Journal of Advances in Modeling Earth Systems*,
705 10, 652-667, <https://doi.org/10.1002/2017MS001234>, 2018.
- 706 McFarlane, N. A.: The Effect of Orographically Excited Gravity Wave Drag on the General
707 Circulation of the Lower Stratosphere and Troposphere, *Journal of Atmospheric*
708 *Sciences*, 44, 1775-1800, [https://doi.org/10.1175/1520-](https://doi.org/10.1175/1520-0469(1987)044<1775:TEOOEG>2.0.CO;2)
709 [0469\(1987\)044<1775:TEOOEG>2.0.CO;2](https://doi.org/10.1175/1520-0469(1987)044<1775:TEOOEG>2.0.CO;2), 1987.
- 710 McLandress, C., Shepherd, T. G., Polavarapu, S., and Beagley, S. R.: Is Missing
711 Orographic Gravity Wave Drag near 60°S the Cause of the Stratospheric Zonal
712 Wind Biases in Chemistry-Climate Models? *Journal of the Atmospheric Sciences*,
713 69, 802-818, <https://doi.org/10.1175/JAS-D-11-0159.1>, 2012.
- 714 Miller, M. J., and Palmer, T. N.: Orographic gravity wave drag: Its parameterization and
715 influence in general circulation and numerical weather prediction models,
716 Presented at the ECWMF Workshop on Observation, Theory and Modelling of
717 Orographic Effects 1, 283-333, 1986.
- 718 Morcrette, J. J., Barker, H. W. J., Cole, N. S., Iacono, M. J., and Pincus, R.: Impact of a
719 New Radiation Package, McRad, in the ECMWF Integrated Forecasting System,
720 *Monthly Weather Review*, 136, 4773-4798,
721 <https://doi.org/10.1175/2008MWR2363.1>, 2008.
- 722 Palmer, T. N., Shutts, G. J., and Swinbank, R.: Alleviation of a systematic westerly bias in
723 general circulation and numerical weather prediction models through an orographic

- 724 gravity wave drag parametrization, Quarterly Journal of the Royal Meteorological
725 Society, 112, 1001-1039, <https://doi.org/10.1002/qj.49711247406>, 1986.
- 726 Scinocca, J., and McFarlane, N.: The parametrization of drag induced by stratified flow
727 over anisotropic orography, Quarterly Journal of the Royal Meteorological Society,
728 126, 2353-2393, <https://doi.org/10.1002/qj.49712656802>, 2000.
- 729 Shen, X., Su, Y., Hu, J., et al.: Development and Operation Transformation of GRAPES
730 Global Middle-range Forecast System, Journal of Applied Meteorological Science,
731 28, 1-10, <https://doi.org/10.11898/1001-7313.20170101>, 2017.
- 732 Shen, X., Wang, J., Li, Z., Chen, D., and Gong, J.: Research and operational development
733 of numerical weather prediction in China, Journal of Meteorological Research, 34,
734 675-698, <https://doi.org/10.1007/s13351-020-9847-6>, 2020.
- 735 [Shen, X. S., Su, Y., Zhang, H. L., et al.: New version of the CMA-GFS dynamical core
736 based on the predictor-corrector time integration scheme, Journal of Meteorological
737 Research, 37, 273-285, <https://doi.org/10.1007/s13351-023-3002-0>, 2023.](#)
- 738 Shutts, G.: Gravity-wave drag parametrization over complex terrain: The effect of critical-
739 level absorption in directional wind-shear, Quarterly Journal of the Royal
740 Meteorological Society, 121, 1005-1021, <https://doi.org/10.1002/qj.49712152504>,
741 1995.
- 742 [Sigmond, M., and Shepherd, T. G.: Compensation between resolved wave driving and
743 parameterized orographic gravity wave driving of the Brewer-Dobson circulation
744 and its response to climate change, Journal of Climate, 27, 5601-5610,
745 <https://doi.org/10.1175/JCLI-D-13-00644.1>, 2014.](#)

- 746 Smith, R. B.: The Influence of Mountains on the Atmosphere, In B. Saltzman (Ed.),
747 Advances in Geophysics (Vol. 21, pp. 87-230): Elsevier, 1979.
- 748 Teixeira, M. A. C.: The physics of orographic gravity wave drag, *Frontiers in Physics*, 2,
749 <https://doi.org/10.3389/fphy.2014.00043>, 2014.
- 750 van Niekerk, A., Vosper, S. B., and Teixeira, M. A. C.: Accounting for the three-
751 dimensional nature of mountain waves: Parametrising partial critical-level filtering,
752 *Quarterly Journal of the Royal Meteorological Society*, 149, 515-536,
753 <https://doi.org/10.1002/qj.4421>, 2023.
- 754 Wei, P., Xu, X., Xue, M., Li, J., Zhao, K., and Zhang, Q.: Complex Terrain Causes Global
755 Model Prediction Biases of 21.7 Zhengzhou Extreme Precipitation, *Science*
756 *Bulletin*, <https://doi.org/10.1016/j.scib.2025.09.015>, 2025.
- 757 Xu, X., Zhou, X., Yang, K., Lu, Y., Zhang, R., Yang, B., Tang, J., Wang, Y.: Reducing
758 Winter Precipitation Biases Over the Western Tibetan Plateau in the Model for
759 Prediction Across Scales (MPAS) With a Revised Parameterization of Orographic
760 Gravity Wave Drag, *Journal of Geophysical Research: Atmospheres*, 128,
761 e2023JD039123, <https://doi.org/10.1029/2023JD039123>, 2023.
- 762 Xu, X., Li, R., Teixeira, M. A. C., and Lu, Y.: On the Momentum Flux of Vertically
763 Propagating Orographic Gravity Waves Excited in Nonhydrostatic Flow over
764 Three-Dimensional Orography, *Journal of the Atmospheric Sciences*, 78, 1807-
765 1822, <https://doi.org/10.1175/JAS-D-20-0370.1>, 2021.
- 766 Xu, X., Teixeira, M. A. C., Xue, M., Lu, Y., and Tang, J.: Impacts of wind profile shear
767 and curvature on the parameterized orographic gravity wave stress in the Weather

- 768 Research and Forecasting model, Quarterly Journal of the Royal Meteorological
769 Society, 146, 3086-3100, <https://doi.org/10.1002/qj.3828>, 2020.
- 770 Xu, X., Wang, Y., and Xue, M.: Momentum Flux and Flux Divergence of Gravity Waves
771 in Directional Shear Flows over Three-Dimensional Mountains, Journal of the
772 Atmospheric Sciences, 69, 3733-3744, <https://doi.org/10.1175/JAS-D-12-044.1>,
773 2012.
- 774 Xu, X., Xue, M., Teixeira, M. A. C., Tang, J., and Wang, Y.: Parameterization of
775 Directional Absorption of Orographic Gravity Waves and Its Impact on the
776 Atmospheric General Circulation Simulated by the Weather Research and
777 Forecasting Model, Journal of the Atmospheric Sciences, 76, 3435-3453,
778 <https://doi.org/10.1175/JAS-D-18-0365.1>, 2019.
- 779 Xu, X., Zhang, R., Teixeira, M. A. C., van Niekerk, A., Xue, M., Lu, Y., Xue, H., Li, R.,
780 Wang, Y.: A Parameterization Scheme Accounting for Nonhydrostatic Effects on
781 the Momentum Flux of Vertically Propagating Orographic Gravity Waves:
782 Formulas and Preliminary Tests in the Model for Prediction Across Scales (MPAS),
783 Journal of the Atmospheric Sciences, 81, 805-817, <https://doi.org/10.1175/JAS-D-23-0020.1>, 2024.
- 785 Xue, H., Shen, X., and Su, Y.: Parameterization of Turbulent Orographic Form Drag and
786 Implementation in GRAPES, Journal of Applied Meteorological Science, 22, 169-
787 181, <http://qikan.camscma.cn/en/article/id/20110206>, 2011.
- 788 Zängl, G.: Orographic Gravity Waves Close to the Nonhydrostatic Limit of Vertical
789 Propagation, Journal of the Atmospheric Sciences, 60, 2045-2063,
790 [https://doi.org/10.1175/1520-0469\(2003\)060<2045:OGWCTT>2.0.CO;2](https://doi.org/10.1175/1520-0469(2003)060<2045:OGWCTT>2.0.CO;2), 2003.

- 791 Zhang, R.: CMA-GFS Model. Zenodo [code], <https://doi.org/10.5281/zenodo.18476721>,
792 2026.
- 793 Zhang, R.: CMA-GFS outputs. Zenodo [data set],
794 <https://doi.org/10.5281/zenodo.18529537>, 2026.
- 795 Zhang, R., Lu, Y., Xu, X., and Wang, Y.: Impacts of wind profile shear and curvature on
796 the parameterized orographic gravity wave stress in a middle atmosphere resolving
797 general circulation model, *Journal of Advances in Modeling Earth Systems*, 17,
798 e2024MS004232, <https://doi.org/10.1029/2024MS004232>, 2025.
- 799 Zhang, R., Xu, X., and Wang, Y.: Impacts of Subgrid Orographic Drag on the Summer
800 Monsoon Circulation and Precipitation in East Asia, *Journal of Geophysical*
801 *Research: Atmospheres*, 125, e2019JD032337,
802 <https://doi.org/10.1029/2019JD032337>, 2020.
- 803 Zhong, S., and Chen, Z.: Improved wind and precipitation forecasts over South China using
804 a modified orographic drag parameterization scheme, *Journal of Meteorological*
805 *Research*, 29, 132-143, <https://doi.org/10.1007/s13351-014-4934-1>, 2015.
806